ELSEVIER

Polymer 43 (2002) 5775–5790

polymer

www.elsevier.com/locate/polymer

Monte Carlo simulation of triblock copolymer thin films

Jie Feng, Eli Ruckenstein*

Department of Chemical Engineering, State University of New York at Buffalo, Buffalo, NY 14260-4200, USA

Received 21 March 2002; received in revised form 5 July 2002; accepted 6 July 2002

Abstract

The morphologies of $A_{m1}B_{2n}A_{m2}$ and $A_mB_nC_p$ triblock copolymer melt films confined between two hard walls are investigated via Monte Carlo simulations on simple cubic lattices. Depending upon the thickness of the film, parallel, perforated, mesh-like and normal lamellae can occur in $A_5B_{10}A_5$ melts. Consequently, no sudden transition occurs between the parallel and normal lamellae. The ratio $m1/m2$ also affects the morphology of the $A_{m1}B_{2n}A_{m2}$ melts. As the ratio is decreased, the microdomains become softer and the boundaries between different phases less sharp. In the $A_mB_nC_m$ systems, lamellar morphologies are present in a wide composition range, when the interaction energies between them and between each of them and vacancies (V) $\epsilon_{AB} = \epsilon_{AC} = \epsilon_{BC} = 0.3$, $\epsilon_{AV} = \epsilon_{BV} = \epsilon_{CV} = 0$, $\epsilon_{AA} = \epsilon_{BB} = \epsilon_{CC} = \epsilon_{VV} = 0$ and the walls are neutral. By increasing the interactions between different kinds of segments from 0.3 to 1, major changes in morphology take place. The preference of the walls for various blocks greatly affects the morphologies and orientations of the microdomains. © 2002 Published by Elsevier Science Ltd.

Keywords: Monte Carlo simulation; Triblock copolymer; Thin film

1. Introduction

In the past decades, the morphologies and phase transitions of block copolymers in bulk have been extensively investigated [1–3]. The chemical bonding of the distinct blocks prevents any macrophase separations; instead, microphase separations at the nano-meter scale occur. The competition between the interaction energies and conformational entropy leads to a variety of complex microstructures at the nano-scale level, dependent on composition and temperature.

Recently, there has been a great deal of interest in studying the thin films of block copolymers, because they can be used as templates for nano-materials [4,5]; it is, therefore, important to understand the pattern formation in such films [6–8]. For the symmetrical A_mB_m diblock copolymer films, the structural periodicity and the orientation of the lamellae have been examined in a number of papers [9–12]. The thickness and the strength of the interactions between the walls and segments have been generally considered as key factors. To control the interactions between surfaces and segments, Huang et al. [13] and Kellogg et al. [14], who investigated experimentally the symmetrical diblock copolymer films confined between two walls, covered the substrates with a random copolymer. The results revealed the existence of lamellae normal to the walls when the latter were neutral. However, parallel lamellae were formed between the two walls when the latter preferred any one of the blocks. Employing Monte Carlo simulations, Sommer et al. [12], Geisinger et al. [15] and Wang et al. [16] studied the microphase structures of diblock copolymers both in bulk and as confined thin films. Their results indicated that lamellar phases occurred in both cases; they were normal to the walls for thin films with neutral walls. Wang et al. noted [16] that for walls that prefer any one of the blocks, the orientation in the film was strongly dependent on the thickness of the film. Matsen [17] employed a self-consistent field approach (SCFT) to examine the stability of parallel, normal, and mixed lamellar phases of confined films of symmetric diblock copolymers. He pointed out that the mixed morphology was slightly unstable in symmetric systems. He also predicted that a stable mixed phase could be formed when a small spontaneous curvature of the A/B interface was generated by an asymmetry in the molecule (f the segment fraction of block A is not equal to 0.5). Besides the symmetry of the diblock system, an external field also affected the microstructure of the asymmetric diblocks. Wang et al. [18] noted that perpendicular cylinders could readily be formed

* Corresponding author. Tel.: +1-716-645-2911x2214; fax: +1-716-645-3822.

E-mail address: feaeliru@acsu.buffalo.edu (E. Ruckenstein).

0032-3861/02/$ - see front matter © 2002 Published by Elsevier Science Ltd.
PII: S0032-3861(02)00439-1

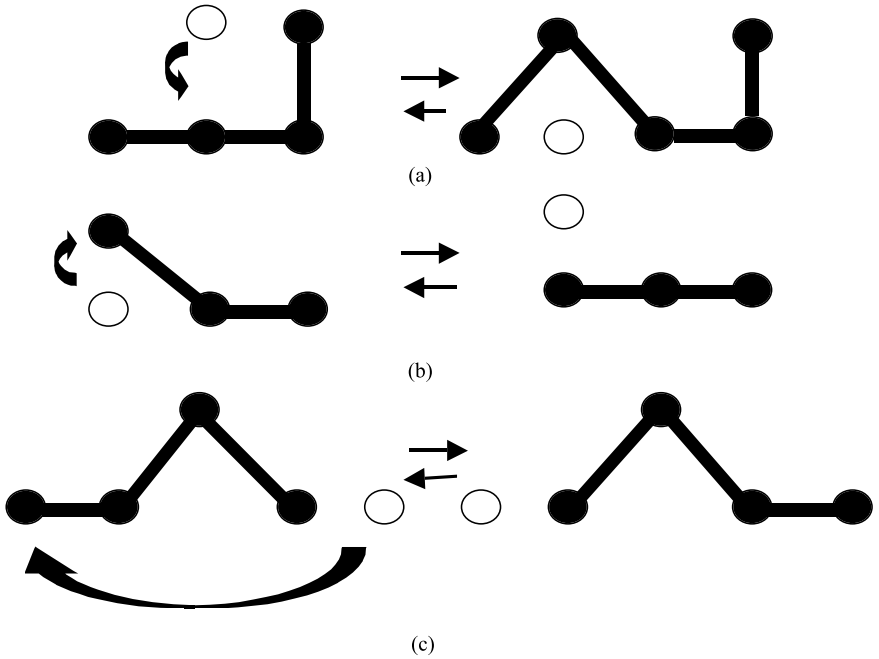

Scheme 1. Motion model.

between two hard surfaces that had a slight energetic preference for the longer blocks. However, parallel cylinders were formed in their simulations when the preference for the longer block became stronger.

In contrast to the diblock systems, much less work was performed on the microstructure of $A_{m1}B_{2n}A_{m2}$ triblock melt systems, since it was considered that their morphologies were similar to the A_mB_n ($m = (m1 + m2)/2$) diblock ones [19]. Most studies about the $A_{m1}B_{2n}A_{m2}$ triblock systems were focused on the loop and bridging fractions chains [20–23]. In experiments regarding the symmetrical triblock systems ($A_mB_{2n}A_m$), Mai et al. [24] found that the lamellar phase of the triblock copolymers was 10% more stretched than that of the corresponding diblock copolymers obtained by splitting the triblock into two diblock ones. Suh et al. [25] noted that the orientation of the cylinders in a confined film was dependent on the film thickness and surface tension. Van Dijk and Van den Berg [26] observed P(styrene) cylinders parallel to the walls in relatively thick (140 nm) films of P(styrene-*b*-butadiene-*b*-styrene) triblock copolymers, and normal to the walls in thin (42 nm) films. Konrad et al. [27] observed mixed morphologies containing both parallel and normal cylinders in films of nonuniform thicknesses. Using a self-consistent field theory (SCFT) approach, Matsen et al. [19,28] investigated the bulk symmetric $A_mB_{2n}A_m$ and asymmetric $A_{m1}B_{2n}A_{m2}$ systems. Their calculations indicated that the triblocks melts remained more ordered at high temperatures than their corresponding diblock counterparts.

Since the microphase separation in $A_mB_nC_p$ triblock systems depends on a large number of parameters, its phase behavior is much more complex than that of the A_mB_n and $A_{m1}B_{2n}A_{m2}$ systems. However, the $A_mB_nC_p$ systems have the potential to become much more useful than the A_mB_n and $A_{m1}B_{2n}A_{m2}$ ones because of the numerous distinct morphologies they possess. Nakazawa and Ohta [29] investigated the microphase separation of the symmetric $A_mB_nC_p$ triblock copolymers ($m = p$) in the strong segregation limit, by extending their theory for the A_mB_n copolymers. By applying the density functional theory combined with the Ohta-Kawasaki free energy expression to the $A_mB_nC_p$ triblock copolymers, Zheng and Wang [30] identified 11 morphologies. Matsen [31] applied the SCFT to the symmetric $A_mB_nC_m$ triblock copolymers, where the A and C blocks were equal in size and the A/B and B/C interactions were the same. Drolet and Fredrickson [32] proposed a numerical implementation of the self-consistent mean field theory involving the parallel screening of self-assembly in complex block copolymer systems. It is interesting to note that the $A_mB_{2n}C_p$ linear triblocks readily produced the 'three-color' (ABCCBA…) lamellar phase, but the $A_{m1}B_{2n}C_pA_{m2}$ architecture did not generate three-color lamellae for the same parameter values. Bohbot-Raviv and Wang [33] presented a new implementation of the SCFT to the block copolymer melts. Using the new method, they found several new stable and metastable microdomain morphologies in the $A_mB_nC_p$ melts. Because of the

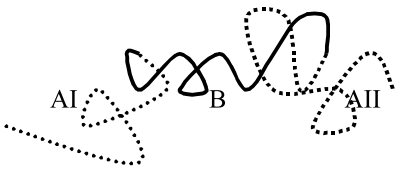

Fig. 1. The triblock copolymer $A_{m1}B_{2n}A_{m2}$ ($m1 < m2$).

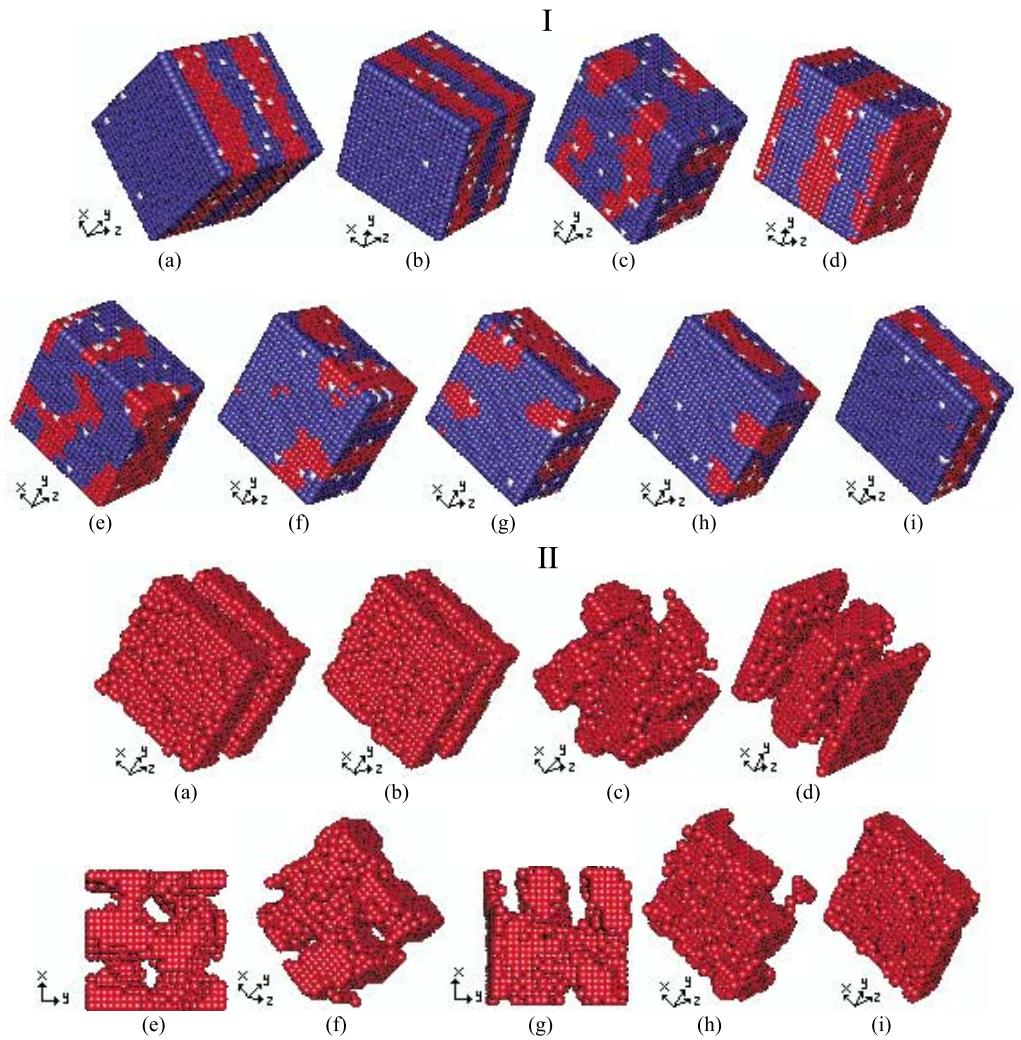

Fig. 2. (I) Microphase morphologies for various thicknesses of the symmetric $A_5B_{10}A_5$ for $\epsilon_{SA} = \epsilon_{SV} = 0$, $\epsilon_{SB} = -0.3$, $\epsilon_{AB} = 0.3$, $\epsilon_{AV} = \epsilon_{BV} = 0$ and $\epsilon_{AA} = \epsilon_{BB} = \epsilon_{VV} = 0$. Red: A segments; Blue: B segments; White: vacancies; (a) $L_Z = 21$, (b) $L_Z = 17$, (c) $L_Z = 16$, (d) $L_Z = 15$, (e) $L_Z = 14$, (f) $L_Z = 13$, (g) $L_Z = 12$, (h) $L_Z = 11$, (i) $L_Z = 10$. (II) Microphase morphologies of A segments for various thicknesses of the symmetric $A_5B_{10}A_5$ for $\epsilon_{SA} = \epsilon_{SV} = 0$, $\epsilon_{SB} = -0.3$, $\epsilon_{AB} = 0.3$, $\epsilon_{AV} = \epsilon_{BV} = 0$ and $\epsilon_{AA} = \epsilon_{BB} = \epsilon_{VV} = 0$. (a) $L_Z = 21$, (b) $L_Z = 17$, (c) $L_Z = 16$, (d) $L_Z = 15$, (e) $L_Z = 14$, (f) $L_Z = 13$, (g) $L_Z = 12$, (h) $L_Z = 11$, (i) $L_Z = 10$.

complexity of the $A_mB_nC_p$ systems, one cannot describe with complete accuracy their microphase separations. Regarding the experimental side, most of the work was focused on the bulk morphologies [34–38]. Matsushita et al. [34] examined the isoprene-*b*-styrene-*b*-2-vinylpyridine (ISP) triblock copolymer, with volume fractions of the three components 0.26, 0.48, 0.26, respectively, and identified a tricontinuous structure. Using the same system, Suzuki et al. [35] identified by transmission electron microscopy and small-angle X-ray scattering microdomains with a tricontinuous double-gyroid structure. Shefelbine et al. [36] examined the asymmetric isoprene-*b*-styrene-*b*-dimethylsiloxane (ISD) triblock copolymer with volume fractions of 0.40, 0.41, 0.19, respectively, and found a core–shell gyroid morphology. The same morphology was identified by Hückstädt et al. [37] for styrene-*b*-1,2-butadiene-*b*-2-vinylpryidine (SBV) triblock copolymer with volume fractions of 0.14, 0.37, 0.49, respectively. Breiner et al. [38] observed a transformation from a lamellar to a knitting pattern morphology when the sample styrene-*b*-butadiene-*b*-methyl methacrylate (SBM) with volume fractions of 0.35, 0.27, 0.38, respectively, was hydrogenated. Using scanning force microscopy, Elbs et al. [39] investigated the styrene-*b*-2-vinylpyridine-*b*-*tert*-butyl methacrylate melt films and obtained results in agreement with the Pickett and Balazs self-consistent-field calculations [40].

In this paper, Monte Carlo simulations will be used to examine the microphase morphologies of the $A_{m1}B_{2n}A_{m2}$ and $A_mB_nC_p$ melt thin films. The paper is organized as follows. In Section 2, a modified bond-fluctuation and vacancy diffusion Monte Carlo algorithm will be described. In Section 3, the microphase morphologies of the $A_{m1}B_{2n}A_{m2}$ triblock melt films will be examined, with the emphasis on the effect of the thickness of the films. In Section 4, the microphase morphologies of the $A_mB_nC_p$ triblock thin films

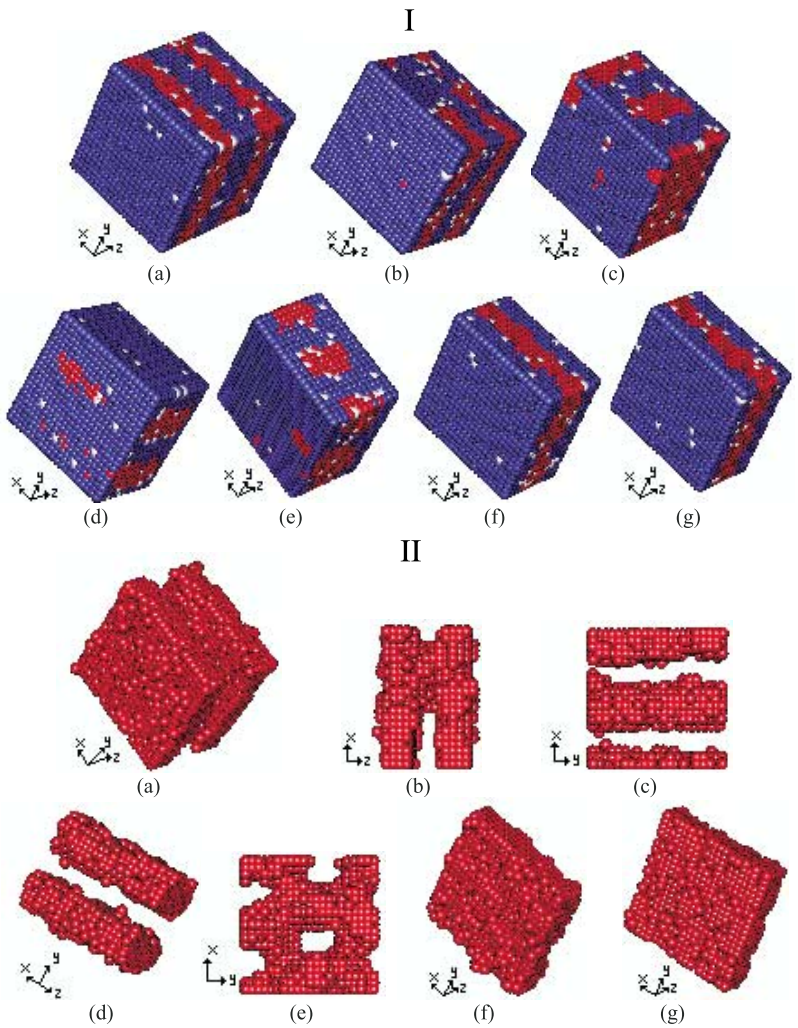

Fig. 3. (I) Microphase morphologies for various thicknesses of the symmetric $A_4B_{12}A_4$ for $\epsilon_{SA} = \epsilon_{SV} = 0$, $\epsilon_{SB} = -0.3$, $\epsilon_{AB} = 0.3$, $\epsilon_{AV} = \epsilon_{BV} = 0$ and $\epsilon_{AA} = \epsilon_{BB} = \epsilon_{VV} = 0$. Red: A segments; Blue: B segments; White: vacancies; (a) $L_Z = 21$, (b) $L_Z = 17$, (c) $L_Z = 15$, (d) $L_Z = 14$, (e) $L_Z = 13$, (f) $L_Z = 12$, (g) $L_Z = 11$. (II) Microphase morphologies of A segments for various thicknesses of the symmetric $A_4B_{12}A_4$ for $\epsilon_{SA} = \epsilon_{SV} = 0$, $\epsilon_{SB} = -0.3$, $\epsilon_{AB} = 0.3$, $\epsilon_{AV} = \epsilon_{BV} = 0$ and $\epsilon_{AA} = \epsilon_{BB} = \epsilon_{VV} = 0$. (a) $L_Z = 21$, (b) $L_Z = 17$, (c) $L_Z = 15$, (d) $L_Z = 14$, (e) $L_Z = 13$, (f) $L_Z = 12$, (g) $L_Z = 11$.

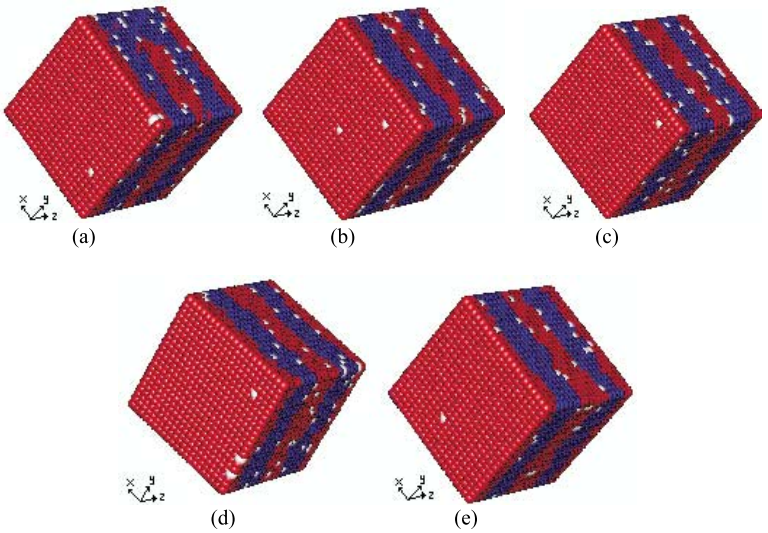

Fig. 4. Microphase morphologies for triblock copolymers with various $m1/m2$ ratios between two hard walls for $\epsilon_{SB} = \epsilon_{SV} = 0$, $\epsilon_{SA} = -0.3$, $\epsilon_{AB} = 0.3$, $\epsilon_{AV} = \epsilon_{BV} = 0$ and $\epsilon_{AA} = \epsilon_{BB} = \epsilon_{VV} = 0$. Red: A segments; Blue: B segments; White: vacancies; (a) $A_1B_{10}A_9$, (b) $A_2B_{10}A_8$, (c) $A_3B_{10}A_7$, (d) $A_4B_{10}A_6$, (e) $A_5B_{10}A_5$.

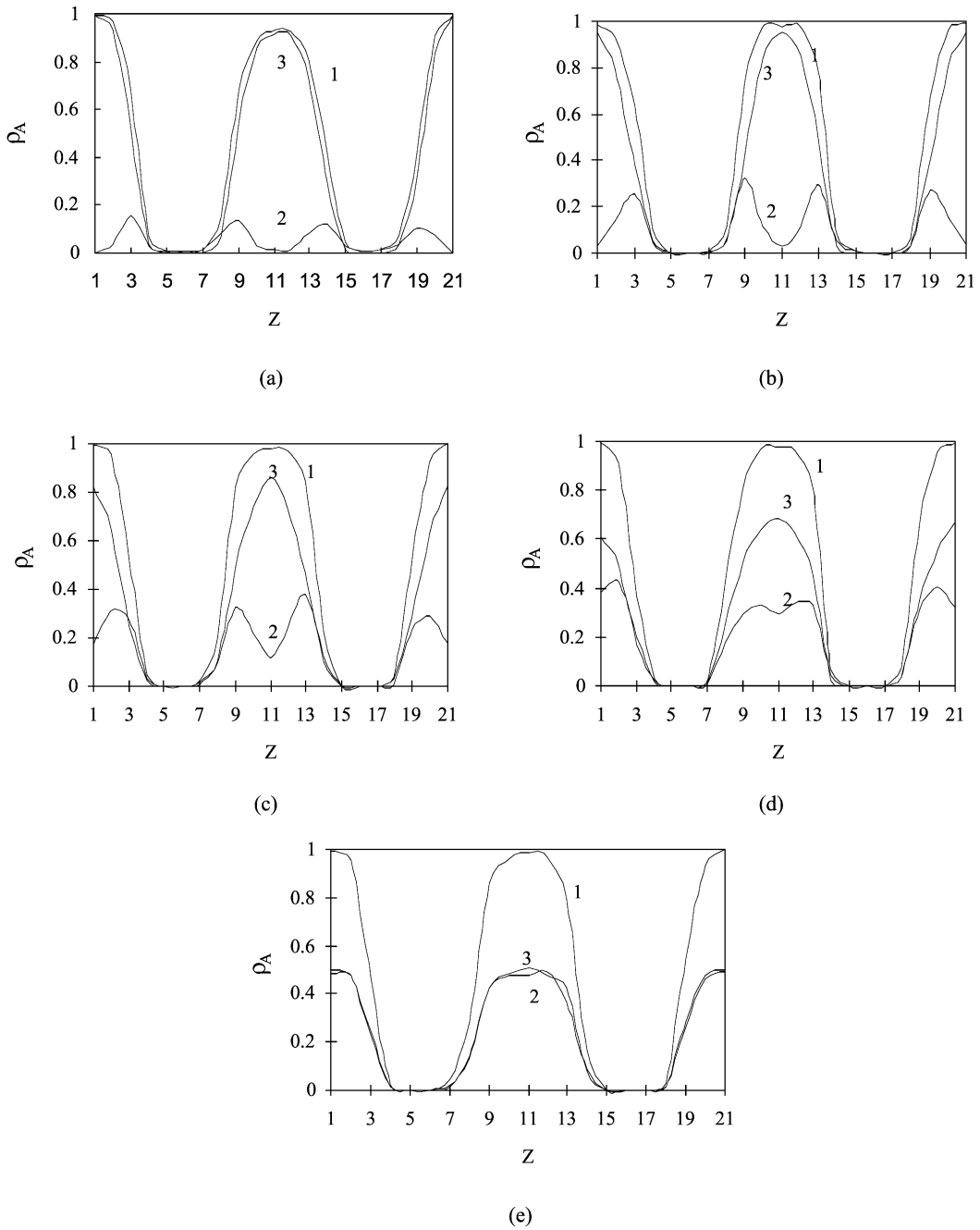

Fig. 5. Density distribution of A segments along the Z-axis for walls that prefer to A segments; $\epsilon_{SB} = \epsilon_{SV} = 0$, $\epsilon_{SA} = -0.3$, $\epsilon_{AB} = 0.3$, $\epsilon_{AV} = \epsilon_{BV} = 0$ and $\epsilon_{AA} = \epsilon_{BB} = \epsilon_{VV} = 0$; (1) Density distribution of total A segments in the polymer chain; (2) density distribution of AI segments; (3) density distribution of AII segments. (a) $A_1B_{10}A_9$, (b) $A_2B_{10}A_8$, (c) $A_3B_{10}A_7$, (d) $A_4B_{10}A_6$, (e) $A_5B_{10}A_5$.

will be presented. In Section 5, we will discuss the effect of the length of the chain. Section 6 will summarize the conclusions.

2. The Monte Carlo simulation algorithm

A cubic lattice model will be used in the simulations. Because of the high concentrations involved, the algorithms that have been successfully employed for dilute polymer solutions could not be effectively extended to the present cases. Larson et al. proposed for the two-dimensional case, the bond fluctuation model [41]. One or several segments were first selected as masters of the motion, followed by the exchange of their positions with vacancies. This kind of exchange is, however, greatly decreased when the bead concentration is high and the number of vacancies is small, because of the low probability to find a vacancy near a selected segment. To improve the efficiency of the simulation, Reiter proposed a free volume diffusion model

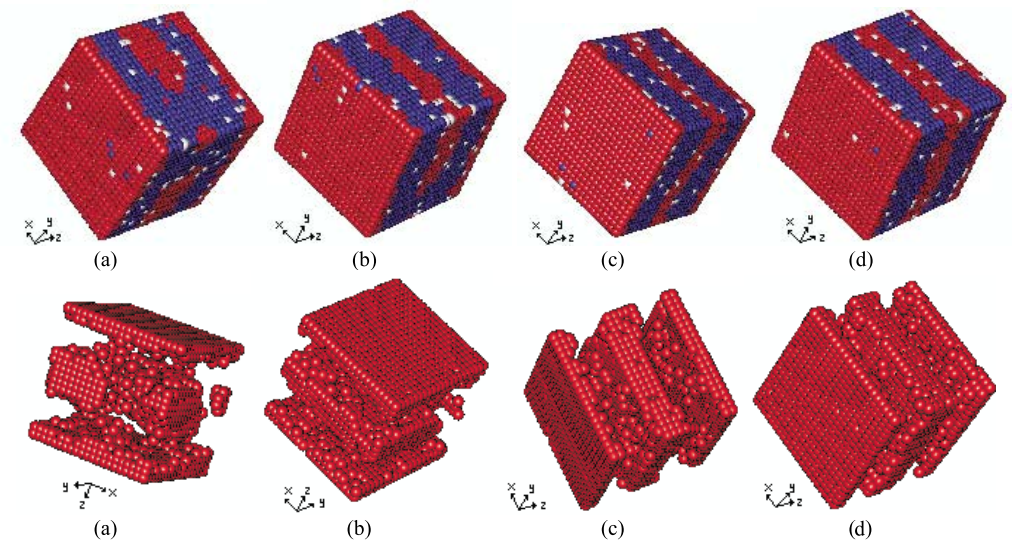

Fig. 6. Microphase morphologies for triblock copolymers with various $m1/m2$ ratios between two hard walls for $\epsilon_{SB} = \epsilon_{SV} = 0$, $\epsilon_{SA} = -0.3$, $\epsilon_{AB} = 0.3$, $\epsilon_{AV} = \epsilon_{BV} = 0$ and $\epsilon_{AA} = \epsilon_{BB} = \epsilon_{VV} = 0$. Red: A segments; Blue: B segments; White: vacancies; (a) $A_1B_{12}A_7$, (b) $A_2B_{12}A_6$, (c) $A_3B_{12}A_5$, (d) $A_4B_{12}A_4$.

[42], in which the master of motion was the vacancy, and Lu and Yang combined the bond fluctuation and the free volume diffusion model [43]. However, the latter combination involved among the motions, the 'middle reptation' (which started from a middle bead, all the beads before being fixed) which violated the detailed balance principle [44]. For reasons emphasized in Ref. [44], we adopted the bond fluctuation combined with the volume diffusion algorithm free of the middle reptation motion (Scheme 1).

3. $A_{m1}B_{2n}A_{m2}$ triblock copolymers melt film

A cubic lattice box of size $L_X \times L_Y \times L_Z$, where L_X, L_Y and L_Z are the box dimensions in the X, Y and Z directions, respectively, was used in the simulations. In the simulation box, each triblock chain consisted of $m1$ segments AI, $m2$ segments AII (the A beads of the shorter block A are denoted AI and those of the longer block A, AII) and $2n$ segments B, with a total segment number $r = m1 + m2 + 2n = 20$ (Fig. 1). Each lattice point is occupied either by a segment or a vacancy. The density of the system was 0.95. In the X and Y directions, periodic boundary conditions were adopted, while in the Z-direction, two impenetrable surfaces were considered to be located at $Z = 0$ and $Z = L_Z + 1$. In the simulations, only the nearest neighbor interactions were taken into account, the repulsive interaction energies between the nearest A–B neighbor segment pairs ϵ_{AB} was taken 0.3, and the other nearest neighbor interaction energies between segments A (ϵ_{AA}), segments B (ϵ_{BB}),

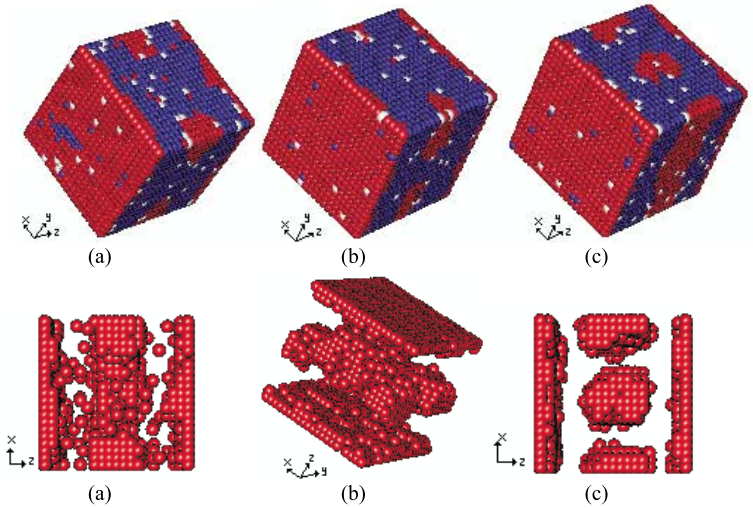

Fig. 7. Microphase morphologies for triblock copolymers with various $m1/m2$ ratios between two hard walls for $\epsilon_{SB} = \epsilon_{SV} = 0$, $\epsilon_{SA} = -0.3$, $\epsilon_{AB} = 0.3$, $\epsilon_{AV} = \epsilon_{BV} = 0$ and $\epsilon_{AA} = \epsilon_{BB} = \epsilon_{VV} = 0$. Red: A segments; Blue: B segments; White: vacancies; (a) $A_1B_{14}A_5$, (b) $A_2B_{14}A_4$, (c) $A_3B_{14}A_3$.

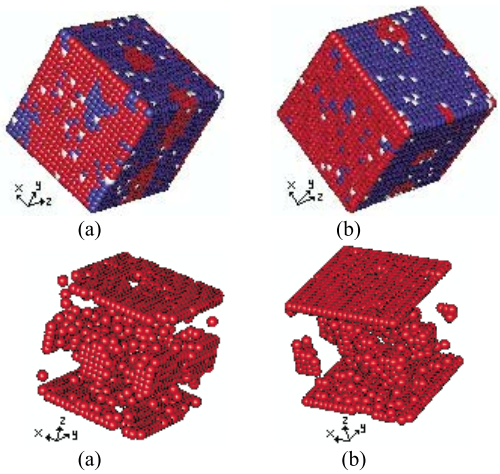

Fig. 8. Microphase morphologies for triblock copolymer with various $m1/m2$ ratios between two hard walls for $\epsilon_{SB} = \epsilon_{SV} = 0$, $\epsilon_{SA} = -0.3$, $\epsilon_{AB} = 0.3$, $\epsilon_{AV} = \epsilon_{BV} = 0$ and $\epsilon_{AA} = \epsilon_{BB} = \epsilon_{VV} = 0$. Red: A segments; Blue: B segments; White: vacancies; (a) $A_1B_{16}A_3$, (b) $A_2B_{16}A_2$.

vacancies (ϵ_{VV}), segments and vacancies (ϵ_{AV} and ϵ_{BV}) were taken equal to zero. Below, the effect of the thickness on the microstructures of the $A_{m1}B_{2n}A_{m2}$ triblock films confined between two walls that prefer either segment A or B (the interaction between one kind of bead and the walls was taken -0.3 and that between the other kind of bead and the walls was taken 0) will be presented.

3.1. The effect of the thickness of the film on microdomain morphologies

It is well known that the symmetric $A_5B_{10}A_5$ triblock copolymer melts microphase separate in bulk in nano-scale lamellar structures as a result of the competition between the interaction energy and the conformational entropy. However, the preference of an external field, such as that generated by walls, for one or the other bead can change the orientation, the shape and the scale of the microdomains. Numerous studies [9,10,15,16] have shown experimentally and theoretically that lamellar morphologies parallel to the walls occurred in copolymer films confined between two hard walls which preferred one kind of the segments of the copolymer chain. On the other hand, lamellar microphase morphologies normal to the walls were found in symmetric copolymer films confined between two neutral hard walls [12–14]. Lambooy et al. [10] observed that the thickness of the lamellae of the diblock copolymer films fluctuated around L_0 (the thickness of the lamellae in the bulk). Wang et al. [16] performing Monte Carlo simulations for A_mB_m diblock copolymer concluded that the orientation of the lamellar morphology was dependent on the L_Z/L_0 ratio when the preference of the walls for A or B was weak. The results obtained by us regarding the symmetric $A_5B_{10}A_5$ triblock copolymer films of various thicknesses confined between two hard preferential walls are presented in Fig. 2(I) and (II). These figures reveal that two rich A parallel lamellae, perforated rich A lamellae, a mesh-like morphology, normal rich A lamellae, a perforated rich A lamella and a layer rich A lamella were formed as L_Z decreased from 21 to 10. Compared with Wang et al.'s simulations for A_mB_m, regarding the effect of the thickness of the film on the microdomain morphology, the present results show that there are a number of complex microdomain morphologies between the parallel and normal lamellae, hence that the transition between the parallel and normal lamellae is not sudden, but more continuous. Furthermore, they revealed that the confined microdomain morphology depends on the extent of frustration induced by the surface-block interactions. Using a cell dynamical system numerical method for a two-dimensional system, Martins et al. [6] studied the effect of thickness on the microdomain morphology of symmetric diblock copolymer films and identified parallel lamellae, normal lamellae and a mixture of both. No complex microdomain morphologies such as the mesh-like one and the perforated lamellae were noted by them. It is clear that the dimensionality of the system affected the microdomain morphologies.

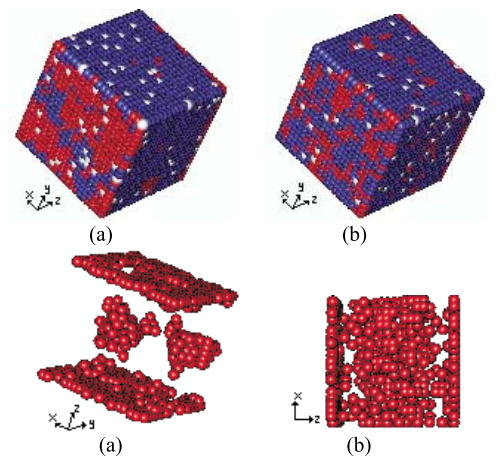

Fig. 9. Microphase morphologies for triblock copolymer with various $m1/m2$ ratios between two hard walls for $\epsilon_{SB} = \epsilon_{SV} = 0$, $\epsilon_{SA} = -0.3$, $\epsilon_{AB} = 0.3$, $\epsilon_{AV} = \epsilon_{BV} = 0$ and $\epsilon_{AA} = \epsilon_{BB} = \epsilon_{VV} = 0$. Red: A segments; Blue: B segments; White: vacancies; (a) A_2B_{18}, (b) $A_1B_{18}A_1$.

Fig. 3(I) and (II) examines the $A_4B_{12}A_4$ melt films confined between two hard walls and show that two rich A parallel lamellae, perforated rich A lamellae, parallel rich A cylinders, a mesh-like morphology, and a layer rich A lamella were formed with decreasing L_Z from 21 to 11.

3.2. Microstructures of $A_{m1}B_{2n}A_{m2}$ triblock copolymers melt films

(a) $\epsilon_{AB} = 0.3$, $\epsilon_{WA} = -0.3$, $\epsilon_{WB} = 0$. In this case, the thickness between the two walls was fixed at 21. Fig. 4 shows that lamellae parallel to the walls occurred for an A segment fraction f_A of 0.5. There are small changes in the morphologies with the variation of the ratio $m1/m2$; more important modifications occurred in the $A_1B_{10}A_9$ triblock system, because the AI beads and the B beads next to AI

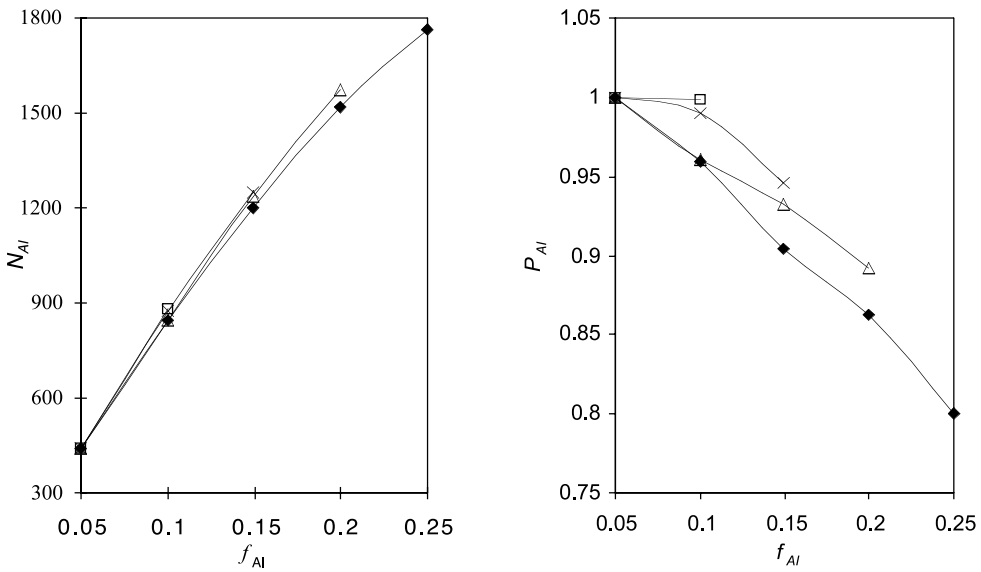

Fig. 10. (a) The relationship between f_{AI} (the volume fraction of AI beads in the chain) and N_{AI} (the number of AI beads at the A/B interfaces) for $\epsilon_{SB} = \epsilon_{SV} = 0$, $\epsilon_{SA} = -0.3$, $\epsilon_{AB} = 0.3$, $\epsilon_{AV} = \epsilon_{BV} = 0$ and $\epsilon_{AA} = \epsilon_{BB} = \epsilon_{VV} = 0$. (b) The relationship between f_{AI} and P_{AI} (the ratio of the number of AI beads at the A/B interface to the total AI beads) for $\epsilon_{SB} = \epsilon_{SV} = 0$, $\epsilon_{SA} = -0.3$, $\epsilon_{AB} = 0.3$, $\epsilon_{AV} = \epsilon_{BV} = 0$ and $\epsilon_{AA} = \epsilon_{BB} = \epsilon_{VV} = 0$; ◆: $f_A = 0.5$; △: $f_A = 0.4$; ×: $f_A = 0.3$; □: $f_A = 0.2$.

more easily penetrated into each other rich regions. Fig. 5 presents the density distributions of the beads A (total A, AI and AII) along the *Z*-axis. As shown in Fig. 5(e), the density distributions along the *Z*-axis of AI and AII are the same because of the same weight of the two blocks A. As the asymmetry in the triblock copolymer increased, the two curves separated. Fig. 5(a)–(d) shows that the AII beads occupied most likely the inner part of the rich A lamellae, while the AI beads had the tendency to accumulate at the A/B interface. The lower the symmetry of the triblock, the higher was the tendency of the shorter A block to move out from the A domain. However, the unfavorable interactions between A and B segments opposed this motion. For this reason, the AI beads had the tendency to accumulate at the interface between A and B, tendency that increased as the

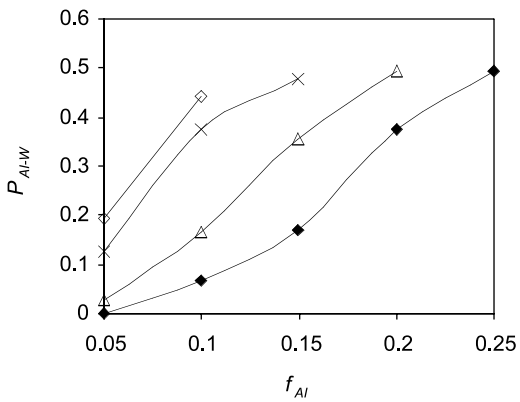

Fig. 11. The ratio P_{AI-W} of occupancy of AI beads at the walls (f_{AI} is the ratio of AI beads in the chain) for $\epsilon_{SB} = \epsilon_{SV} = 0$, $\epsilon_{SA} = -0.3$, $\epsilon_{AB} = 0.3$, $\epsilon_{AV} = \epsilon_{BV} = 0$ and $\epsilon_{AA} = \epsilon_{BB} = \epsilon_{VV} = 0$; ◆: $f_A = 0.5$; △: $f_A = 0.4$; ×: $f_A = 0.3$; □: $f_A = 0.2$.

symmetry became lower. Matsen arrived at a similar conclusion for a bulk system via the SCFT [28].

As shown in Fig. 6, for $f_A = 0.4$, the microdomain morphology away from the walls changed from perforated lamellae to complete lamellae as the symmetry of the system increased. For $f_A = 0.3$ (Fig. 7), some sites on the walls were occupied by the B beads because of the smaller fraction of A beads in the chain and the weak attractive interactions between the walls and the A beads. Away from the walls, there are rich A cylindrical microdomains. Comparing the $A_1B_{14}A_5$ and $A_3B_{14}A_3$ triblock copolymer films (Fig. 7), one can see that the boundaries between various phases were slightly less sharp in the former because the AI beads of the chain penetrated into the rich B phase. In addition, the microdomains became slightly softer as the symmetry of the chain of the triblock copolymer decreased. By decreasing f_A to 0.2 (Fig. 8), rich A cylindrical microdomains could be still observed away from the walls, but the radius of the cylinders became smaller than for $f_A = 0.3$. The interfaces between the rich A and B phases were sharper for the $A_2B_{16}A_2$ triblock than for the $A_1B_{16}A_3$ one. Fig. 9 reveals that, for the $A_1B_{18}A_1$ triblock, phase separation occurred mainly near the walls. However, in the A_2B_{18} diblock copolymer, a complete microphase separation occurred also in the films and not only near the walls. This happened because the constrain imposed by the two block-junctions of the triblock copolymer decreased the conformational entropy compared to that of a diblock copolymer of the same length and composition.

As expected (Fig. 10(a)), N_{AI}, the number of AI beads at

the A/B interface, increased as the fraction of A beads increased. A bead A was considered located at the above interface, when it contacted at least one bead B. For the same fraction of AI beads in the chains and regardless of the fraction of total A segments in the system, there were nearly the same number of beads AI at the A/B interface. Even though the number of AI beads located at the A/B interface increased as the fraction of AI beads in the chain increased (Fig. 10(b)), the ratio between the number of AI beads at the A/B interfaces to that of the total AI beads decreased. This indicates that the increase in the ratio $m1/m2$ reduced the ratio of AI beads at the A/B interfaces to the total AI beads. For $f_A = 0.2$ (Fig. 10(b)), most of the AI beads were located at the A/B interface because of the small size of the microdomains A and because almost every A bead contacted B beads. Fig. 11 shows that the percentage of AI segments at the walls increased when the f_A increased at constant f_{AI}. The ratio of $m1/m2$ of the system decreased and for this reason the fraction of AI segments located at the wall became smaller.

(b) $\epsilon_{AB} = 0.3$, $\epsilon_{WA} = 0$, $\epsilon_{WB} = -0.3$. As shown in Fig. 12, the morphologies for $f_A = 0.5$ were lamellar, and rich B layers were located near the walls because of the preference of the walls for the B segments. For reasons similar to those mentioned in the previous section, in the asymmetric triblock copolymer, the AI segments could easily penetrate into the rich B microdomain. For instance, for the $A_1B_{10}A_9$ triblock copolymer, several AI beads were located on the walls for $\epsilon_{WB} = -0.3$ and $\epsilon_{WA} = 0$. Fig. 13 reveals that the likelihood for the AI segments to be located at the A/B interfaces (the ratio between those located at the A/B interface and their total number) was larger than that for the AII segments. This occurred because the AI segments were less constrained than the AII ones. The lower the symmetry of the chain, the greater was the above tendency. As shown in Fig. 14, when f_A was decreased from 0.5 to 0.4, the lamellar morphology still persisted for the symmetric $A_4B_{12}A_4$ triblock copolymer. However, as the ratio $m1/m2$ decreased, the boundary between the microdomains A and B became less sharp and the rich A microdomains changed to perforated lamellae. Furthermore, a number of A beads became located at the walls, as the ratio of $m1/m2$ of the chain decreased. Fig. 15(b) and (c) shows that in the $A_2B_{14}A_4$ and $A_3B_{14}A_3$ triblock films, two series of rich A cylinders normal to each other and parallel to the walls were formed. In the $A_1B_{14}A_5$ triblock films (Fig. 15(a)), the two series of cylinders were no longer present; instead, irregular A microdomains appeared. When f_A was further decreased to 0.2 (Fig. 16), the rich A cylinders parallel to the walls changed to normal cylinders, particularly for the $A_1B_{16}A_3$ triblock films. Fig. 17 shows that, compared to the A_2B_{18} diblock copolymer films, no phase separation occurred in the $A_1B_{18}A_1$ triblock films, which possessed a more random structure.

As shown in Fig. 18, as the fraction of AI beads in the chain increased, the number of AI beads at the A/B interface also increased, but their fraction at interface with respect to the total number decreased. By comparing Figs. 18 and 10, one can conclude that for the same composition and molecular architecture, the number of AI beads at the A/B interface for walls that preferred the B segments was smaller than for those which preferred the A segments. Fig. 19 indicates that the AI segments could easily penetrate into the rich B lamellae near the walls when AI possessed a single A bead.

4. The microstructures of the $A_mB_nC_p$ triblock copolymers melt film

No complete examination of the morphologies of the $A_mB_nC_p$ triblock copolymer melts was yet carried out

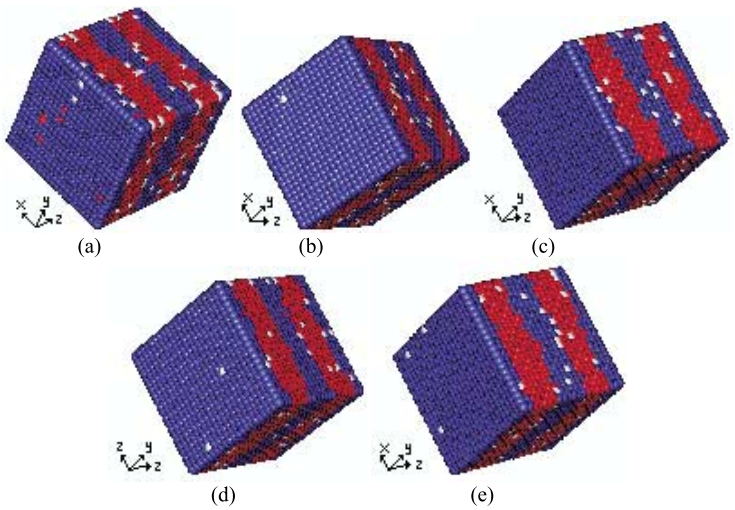

Fig. 12. Microphase morphologies for triblock copolymer with various $m1/m2$ ratios between two hard walls for $\epsilon_{SA} = \epsilon_{SV} = 0$, $\epsilon_{SB} = -0.3$, $\epsilon_{AB} = 0.3$, $\epsilon_{AV} = \epsilon_{BV} = 0$ and $\epsilon_{AA} = \epsilon_{BB} = \epsilon_{VV} = 0$. Red: A segments; Blue: B segments; White: vacancies; (a) $A_1B_{10}A_9$, (b) $A_2B_{10}A_8$, (c) $A_3B_{10}A_7$, (d) $A_4B_{10}A_6$, (e) $A_5B_{10}A_5$.

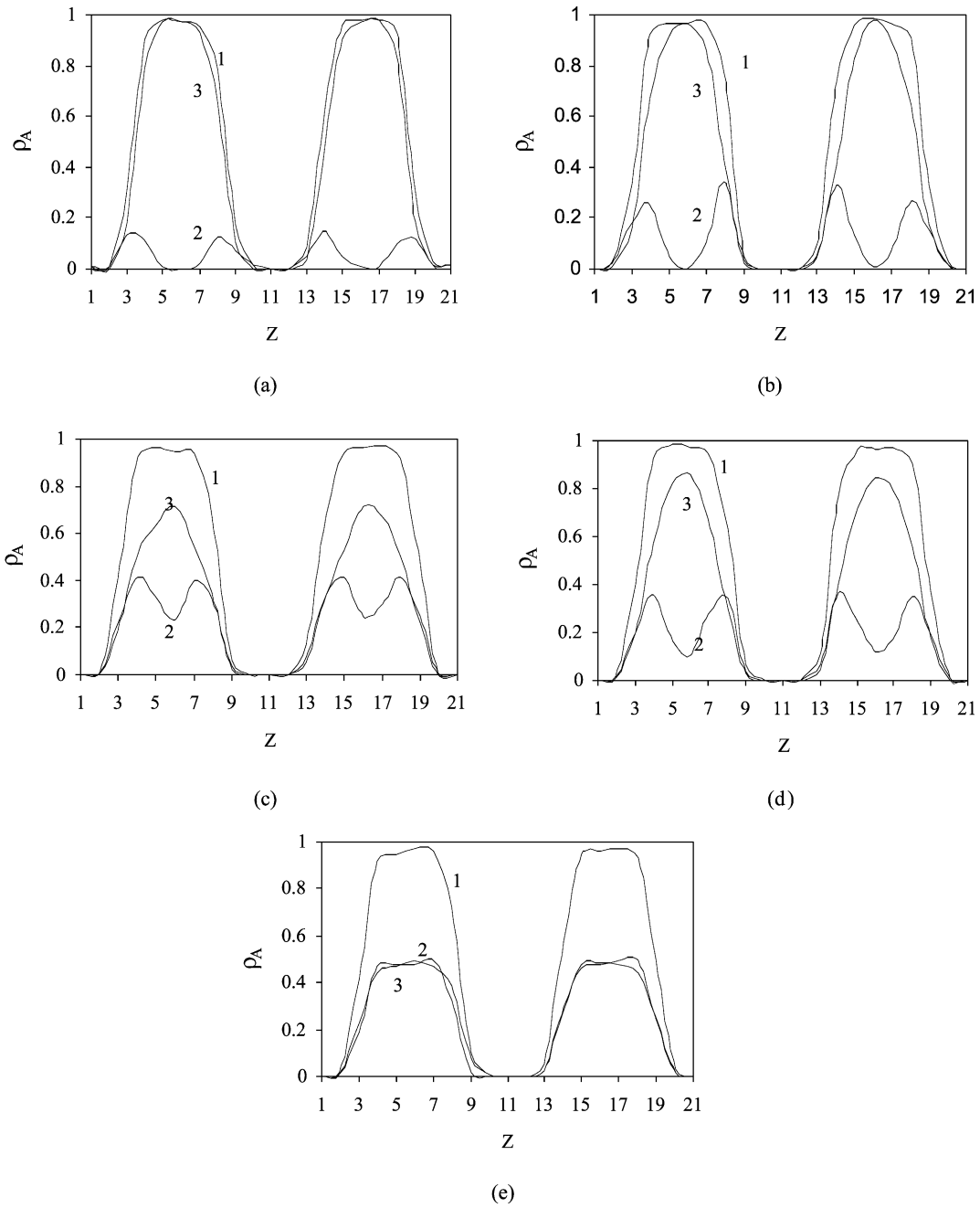

Fig. 13. Density distribution of A segments along the *Z*-axis for walls which prefer B segments; (1) Density distribution of total A segments in polymer chain; (2) density distribution of AI segments; (3) density distribution of AII segments. (a) $A_1B_{10}A_9$, (b) $A_2B_{10}A_8$, (c) $A_3B_{10}A_7$, (d) $A_4B_{10}A_6$, (e) $A_5B_{10}A_5$.

because of its complexity. In this section, the morphologies of the symmetric $A_mB_nC_p$ triblock copolymer films, with $m = p$ and $m + n + p = 15$, confined between two hard walls, will be presented.

4.1. Ultra-thin films with $L_Z = 3$

Phan and Fredrickson [45] concluded that for $0 \leq f_B \leq 0.69$, the bulk triblock copolymer melts exhibit lamellar structures. Fig. 20 for an ultra-thin film shows that, for $\epsilon_{AB} = \epsilon_{AC} = \epsilon_{BC} = 0.3$, $\epsilon_{AV} = \epsilon_{BV} = \epsilon_{CV} = 0$, $\epsilon_{AA} = \epsilon_{BB} = \epsilon_{CC} = \epsilon_{VV} = 0$, and neutral walls, ABCCBA type lamellae were generated in the $A_3B_9C_3$, $A_4B_7C_4$, $A_5B_5C_5$ and $A_6B_3C_6$ systems and microdomains consisting of A and C beads were dispersed into a B continuous phase in the $A_2B_{11}C_2$ system. Matsen [31] concluded that, as in the diblock melts, the composition of the triblock ones controls the bulk morphology and that the interactions affect mainly the extent of segregation. In contrast, Breiner et al. [38] pointed out that not only the composition but also the relative incompatibilities between the segments affect the bulk morphologies. As shown in Fig. 21, the morphology of

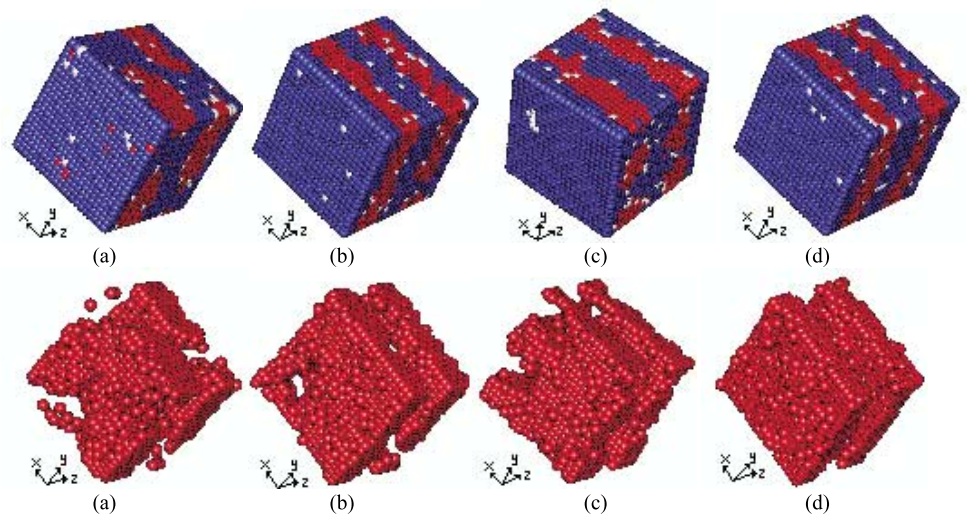

Fig. 14. Microphase morphologies for triblock copolymers with various $m1/m2$ ratios between two hard walls for $\epsilon_{SA} = \epsilon_{SV} = 0$, $\epsilon_{SB} = -0.3$, $\epsilon_{AB} = 0.3$, $\epsilon_{AV} = \epsilon_{BV} = 0$ and $\epsilon_{AA} = \epsilon_{BB} = \epsilon_{VV} = 0$. Red: A segments; Blue: B segments; White: vacancies; (a) $A_1B_{12}A_7$, (b) $A_2B_{12}A_6$, (c) $A_3B_{12}A_5$, (d) $A_4B_{12}A_4$.

an ultra-thin film exhibited major changes and the ABCCBA lamellae disappeared when ϵ_{AB}, ϵ_{AC} and ϵ_{BC} were increased from 0.3 to unity. For $A_7B_3C_7$ with $\epsilon_{AC} = 0.1$ and $\epsilon_{AB} = \epsilon_{BC} = 0.5$ (Fig. 22(a)), a 'tricolor checkerboard-like' morphology was formed, while for the $A_2B_2C_9$ system with $\epsilon_{AC} = 0.5$ and $\epsilon_{AB} = \epsilon_{BC} = 0.1$, A microdomains encircled by B segments were dispersed in the C continuous phase (Fig. 22(b)).

4.2. $L_Z = 20$

To examine the effect of the walls on the morphology, various interaction energies between the walls and the copolymer segments were considered. For neutral walls (Fig. 23), alternate ABCCBA lamellae normal to the walls were generated. When the wall placed at $Z = 0$ attracted the A segments ($\epsilon_{S0A} = -0.3$, $\epsilon_{S0B} = 0$, $\epsilon_{S0C} = 0$) and that placed at $Z = 21$ attracted the C segments ($\epsilon_{S21A} = 0$, $\epsilon_{S21B} = 0$, $\epsilon_{S21C} = -0.3$), alternate ABCCBA lamellae parallel to the walls were formed (Fig. 24(a)) with A and C segments covering the walls at $Z = 0$ and 21, respectively. By increasing the strength of the attraction of the walls for the A and C segments to $\epsilon_{S0A} = -1$ and $\epsilon_{S21C} = -1$, the morphology remained unchanged (Fig. 24(d)). When both walls attracted the A segments ($\epsilon_{S0A} = \epsilon_{S21A} = -0.3$, $\epsilon_{S0B} = \epsilon_{S21B} = \epsilon_{S0C} = \epsilon_{S21C} = 0$), they were occupied by them (Fig. 24(c)). However, the morphology away from the walls became irregular because of the frustration induced by the walls. By increasing ϵ_{S0A} and ϵ_{S21A} to -1, the two walls became more strongly occupied by A (Fig. 24(f)). It should be noted that, when the walls preferred B ($\epsilon_{S0B} = \epsilon_{S21B} = -0.3$, $\epsilon_{S0A} = \epsilon_{S21A} = \epsilon_{S0C} = \epsilon_{S21C} = 0$), the ABCCBA lamellar structure persisted because of the special location of the block B in the chain (Fig. 24(b)). As the preference of the wall for the B segments increased, the A and C segments were gradually

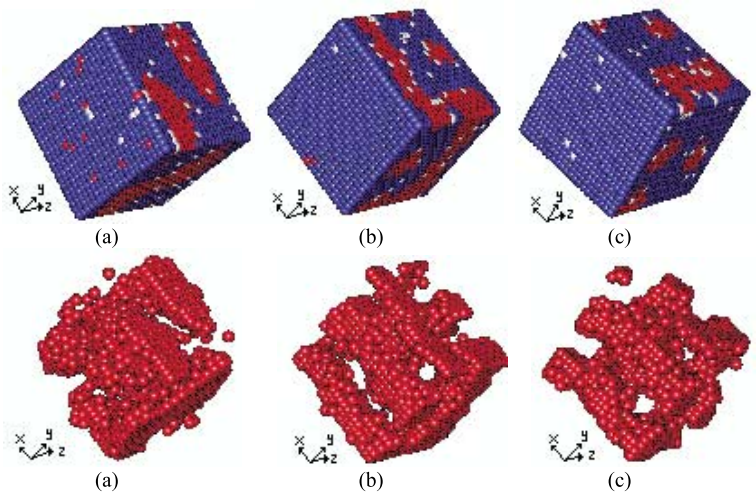

Fig. 15. Microphase morphologies for triblock copolymers with various $m1/m2$ ratios between two hard walls for $\epsilon_{SA} = \epsilon_{SV} = 0$, $\epsilon_{SB} = -0.3$, $\epsilon_{AB} = 0.3$, $\epsilon_{AV} = \epsilon_{BV} = 0$ and $\epsilon_{AA} = \epsilon_{BB} = \epsilon_{VV} = 0$. Red: A segments; Blue: B segments; White: vacancies; (a) $A_1B_{14}A_5$, (b) $A_2B_{14}A_4$, (c) $A_3B_{14}A_3$.

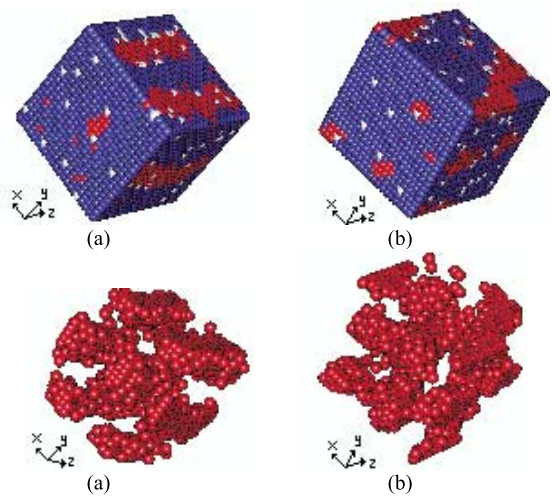

Fig. 16. Microphase morphologies for triblock copolymers with various $m1/m2$ ratios between two hard walls for $\epsilon_{SA} = \epsilon_{SV} = 0$, $\epsilon_{SB} = -0.3$, $\epsilon_{AB} = 0.3$, $\epsilon_{AV} = \epsilon_{BV} = 0$ and $\epsilon_{AA} = \epsilon_{BB} = \epsilon_{VV} = 0$. Red: A segments; Blue: B segments; White: vacancies; (a) $A_1B_{16}A_3$, (b) $A_2B_{16}A_2$.

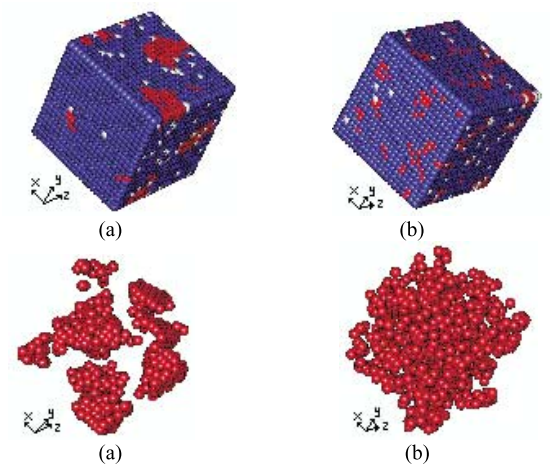

Fig. 17. Microphase morphologies for copolymers with various architectures between two hard walls for $\epsilon_{SA} = \epsilon_{SV} = 0$, $\epsilon_{SB} = -0.3$, $\epsilon_{AB} = 0.3$, $\epsilon_{AV} = \epsilon_{BV} = 0$ and $\epsilon_{AA} = \epsilon_{BB} = \epsilon_{VV} = 0$. Red: A segments; Blue: B segments; White: vacancies; (a) A_2B_{18}, (b) $A_1B_{18}A_1$.

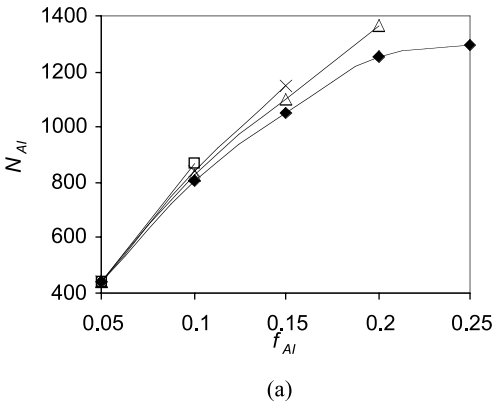

(a)

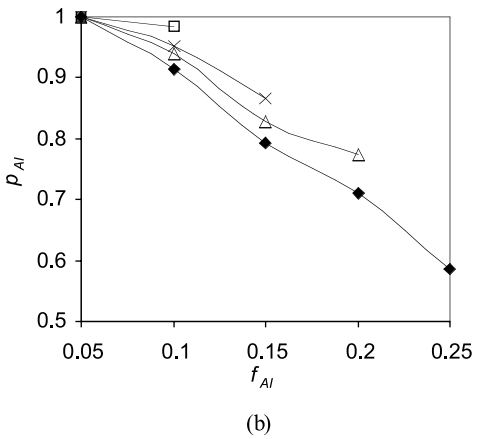

(b)

Fig. 18. (a) The relationship between f_{AI} (the volume fraction of AI beads in the chain) and N_{AI} (the number of AI beads at the A/B interface) for $\epsilon_{SA} = \epsilon_{SV} = 0$, $\epsilon_{SB} = -0.3$, $\epsilon_{AB} = 0.3$, $\epsilon_{AV} = \epsilon_{BV} = 0$ and $\epsilon_{AA} = \epsilon_{BB} = \epsilon_{VV} = 0$. (b) The relationship between f_{AI} and P_{AI} (the ratio of the number of AI beads at the A/B interfaces to the total AI beads) for $\epsilon_{SA} = \epsilon_{SV} = 0$, $\epsilon_{SB} = -0.3$, $\epsilon_{AB} = 0.3$, $\epsilon_{AV} = \epsilon_{BV} = 0$ and $\epsilon_{AA} = \epsilon_{BB} = \epsilon_{VV} = 0$; ◆: $f_A = 0.5$; △: $f_A = 0.4$; ×: $f_A = 0.3$; □: $f_A = 0.2$.

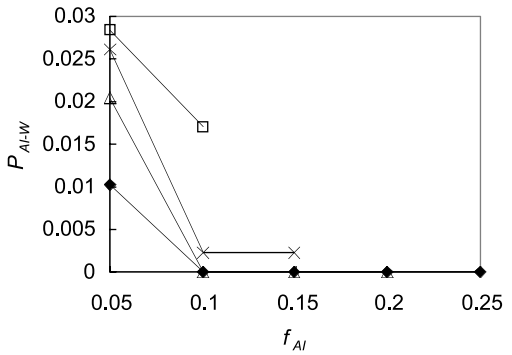

Fig. 19. The ratio of occupancies of AI beads at the walls (f_{AI} is the ratio of AI beads in the chain) for $\epsilon_{SA} = \epsilon_{SV} = 0$, $\epsilon_{SB} = -0.3$, $\epsilon_{AB} = 0.3$, $\epsilon_{AV} = \epsilon_{BV} = 0$ and $\epsilon_{AA} = \epsilon_{BB} = \epsilon_{VV} = 0$; ◆: $f_A = 0.5$; △: $f_A = 0.4$; ×: $f_A = 0.3$; □: $f_A = 0.2$.

expelled. For $\epsilon_{S0B} = \epsilon_{S21B} = -1$, the two walls were mainly occupied by the B segments and normal microdomains were formed away from the two walls (Fig. 24(e)). When the ϵ_{S0B} and ϵ_{S21B} were strengthen to -2.0, the A and C segments were removed from the two walls completely, but the microdomain morphologies away from the two walls remained unchanged (Fig. 25). On the basis of the SCFT, Pickett and Balazs [40] arrived at the same conclusions. Furthermore, Elbs et al. [39] observed experimentally such structures for the P(styrene-*b*-2-vinylpyridine-*b*-*tert*-butyl methacrylate) films.

5. The effect of the length of the chain

In order to evaluate the effect of the length of the polymer chain, simulations have also been carried out with the chains $A_{10}B_{20}A_{10}$ and $A_{10}B_{10}C_{10}$ and the results obtained are presented in Figs. 26 and 27, where they are compared to those obtained for $A_5B_{10}A_5$ and $A_5B_5C_5$, respectively. The comparison reveals that the morphologies are the same, but, as expected, the sizes of the microdomains are different.

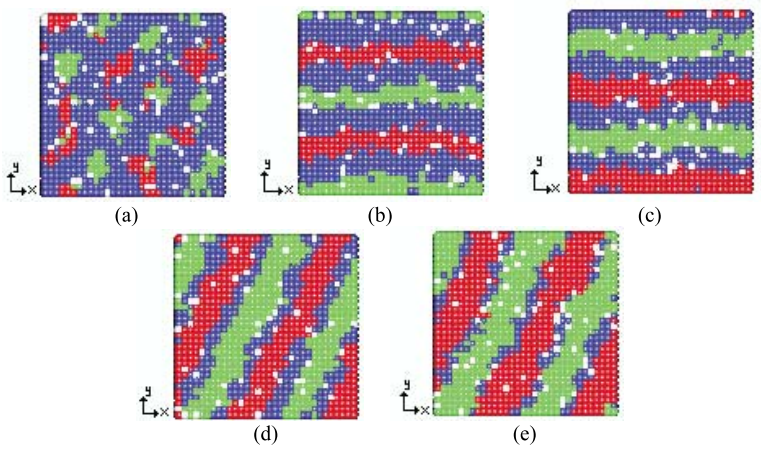

Fig. 20. Microdomain morphologies of the symmetric $A_mB_nC_m$ triblock copolymers for an ultra-thin film ($L_Z = 3$) and $\epsilon_{AB} = \epsilon_{AC} = \epsilon_{BC} = 0.3$, $\epsilon_{AA} = \epsilon_{BB} = \epsilon_{CC} = \epsilon_{VV} = 0$, $\epsilon_{AV} = \epsilon_{BV} = \epsilon_{CV} = 0$, and $\epsilon_{SA} = \epsilon_{SB} = \epsilon_{SC} = \epsilon_{SV} = 0$; Red: A segments; Blue: B segments; Green: C segments; White: vacancies; (a) $A_2B_{11}C_2$, (b) $A_3B_9C_3$, (c) $A_4B_7C_4$, (d) $A_5B_5C_5$, (e) $A_6B_3C_6$.

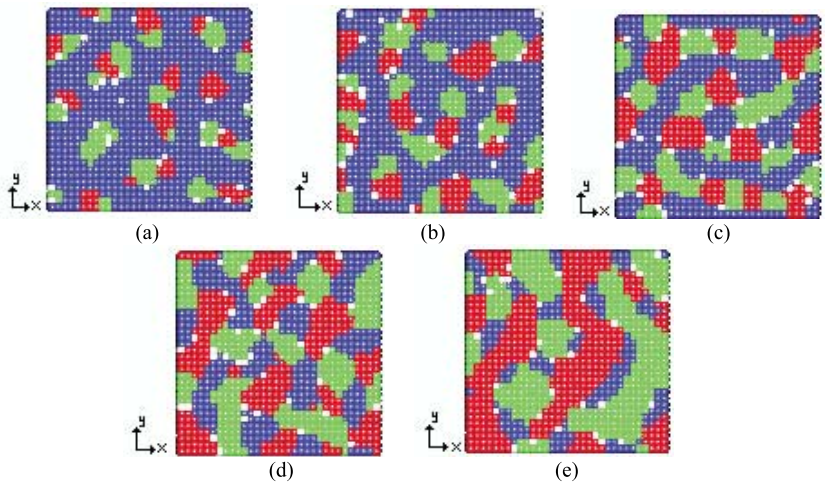

Fig. 21. Microdomain morphologies of the symmetric $A_mB_nC_m$ triblock copolymers for an ultra-thin film ($L_Z = 3$) and $\epsilon_{AB} = \epsilon_{AC} = \epsilon_{BC} = 1$, $\epsilon_{AA} = \epsilon_{BB} = \epsilon_{CC} = \epsilon_{VV} = 0$, $\epsilon_{AV} = \epsilon_{BV} = \epsilon_{CV} = 0$ and $\epsilon_{SA} = \epsilon_{SB} = \epsilon_{SC} = \epsilon_{SV} = 0$; Red: A segments; Blue: B segments; Green: C segments; White: vacancies; (a) $A_2B_{11}C_2$, (b) $A_3B_9C_3$, (c) $A_4B_7C_4$, (d) $A_5B_5C_5$, (e) $A_6B_3C_6$.

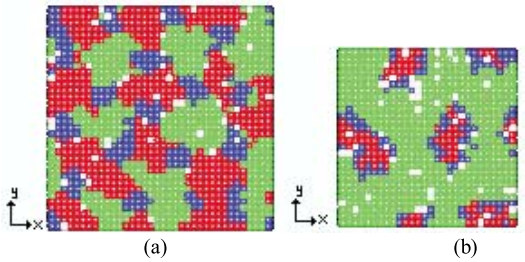

Fig. 22. Microdomain morphologies of A_mB_nC triblock copolymers for an ultra-thin film ($L_Z = 3$) and $\epsilon_{AA} = \epsilon_{BB} = \epsilon_{CC} = \epsilon_{VV} = 0$, $\epsilon_{AV} = \epsilon_{BV} = \epsilon_{CV} = 0$, and $\epsilon_{SA} = \epsilon_{SB} = \epsilon_{SC} = \epsilon_{SV} = 0$; Red: A segments; Blue: B segments; Green: C segments; White: vacancies; (a) $A_7B_3C_7$ with $\epsilon_{AC} = 0.1$ and $\epsilon_{AB} = \epsilon_{BC} = 0.5$; (b) $A_2B_2C_9$ with $\epsilon_{AC} = 0.5$ and $\epsilon_{AB} = \epsilon_{BC} = 0.1$.

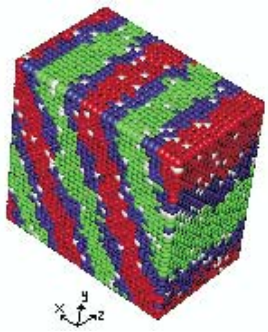

Fig. 23. Microdomain morphology of an $A_5B_5C_5$ triblock copolymers film confined between two neutral walls for $\epsilon_{AB} = \epsilon_{AC} = \epsilon_{BC} = 0.3$, $\epsilon_{AA} = \epsilon_{BB} = \epsilon_{CC} = \epsilon_{VV} = 0$, $\epsilon_{AV} = \epsilon_{BV} = \epsilon_{CV} = 0$ and $\epsilon_{SA} = \epsilon_{SB} = \epsilon_{SC} = \epsilon_{SV} = 0$; Red: A segments; Blue: B segments; Green: C segments; White: vacancies.

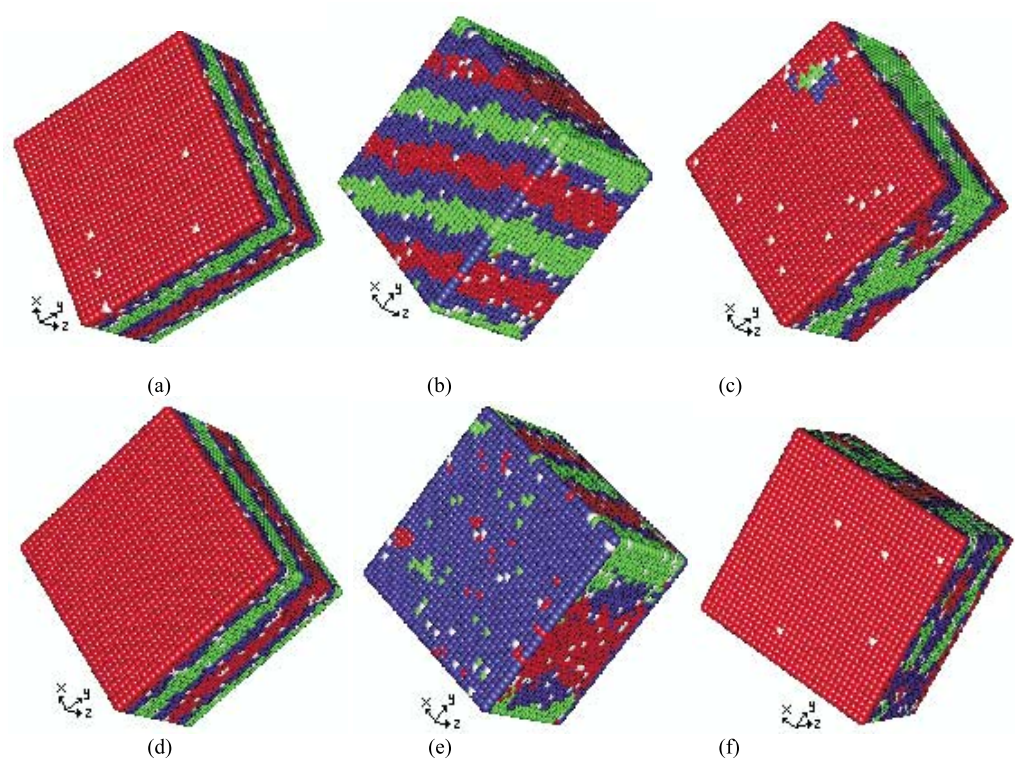

Fig. 24. Microdomain morphologies of $A_5B_5C_5$ triblock copolymers films for various wall conditions and $\epsilon_{AB} = \epsilon_{AC} = \epsilon_{BC} = 0.3$, $\epsilon_{AA} = \epsilon_{BB} = \epsilon_{CC} = \epsilon_{VV} = 0$, $\epsilon_{AV} = \epsilon_{BV} = \epsilon_{CV} = 0$; Red: A segments; Blue: B segments; Green: C segments; White: vacancies; (a) $\epsilon_{S0A} = -0.3$, $\epsilon_{S0B} = \epsilon_{S0C} = 0$, $\epsilon_{S21C} = -0.3$, $\epsilon_{S21A} = \epsilon_{S21B} = 0$; (b) $\epsilon_{S0B} = \epsilon_{S21B} = -0.3$, $\epsilon_{S0A} = \epsilon_{S0C} = 0$, $\epsilon_{S21A} = \epsilon_{S21C} = 0$; (c) $\epsilon_{S0A} = \epsilon_{S21A} = -0.3$, $\epsilon_{S0B} = \epsilon_{S0C} = 0$, $\epsilon_{S21B} = \epsilon_{S21C} = 0$; (d) $\epsilon_{S0A} = -1$, $\epsilon_{S0B} = \epsilon_{S0C} = 0$, $\epsilon_{S21C} = -1$, $\epsilon_{S21A} = \epsilon_{S21B} = 0$; (e) $\epsilon_{S0B} = \epsilon_{S21B} = -1$, $\epsilon_{S0A} = \epsilon_{S0C} = 0$, $\epsilon_{S21A} = \epsilon_{S21C} = 0$; (f) $\epsilon_{S0A} = \epsilon_{S21A} = -1$, $\epsilon_{S0B} = \epsilon_{S0C} = 0$, $\epsilon_{S21B} = \epsilon_{S21C} = 0$.

6. Conclusions

In this paper, the morphologies of the $A_{m1}B_{2n}A_{m2}$ and $A_mB_nC_p$ triblock copolymer films confined between two hard walls were investigated via Monte Carlo simulations on a simple cubic lattice. The simulation results are in agreement with the self-consistent field theoretical results from Refs. [28,40].

The simulations revealed that the confined morphology was dependent on the extent of frustration induced by the wall-block interactions. When the thickness of the films was changed, several morphologies, such as parallel lamellae, perforated lamellae, mesh-like morphologies and normal lamellae were successively generated. The symmetry of the $A_{m1}B_{2n}A_{m2}$ triblock copolymer chain also affected the morphology and distribution of the beads. As the symmetry with respect to A was reduced, the microdomains became softer and the boundaries between different phases became

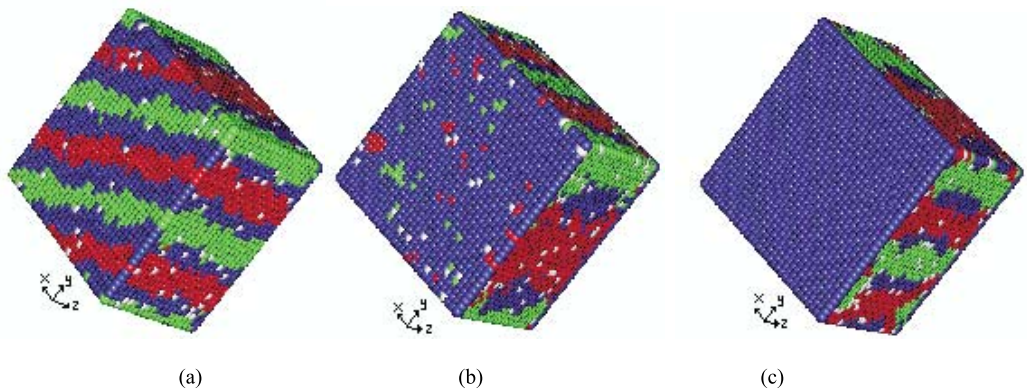

Fig. 25. Microdomain morphologies of $A_5B_5C_5$ triblock copolymers films for various wall conditions and $\epsilon_{AB} = \epsilon_{AC} = \epsilon_{BC} = 0.3$, $\epsilon_{AA} = \epsilon_{BB} = \epsilon_{CC} = \epsilon_{VV} = 0$, $\epsilon_{AV} = \epsilon_{BV} = \epsilon_{CV} = 0$, $\epsilon_{SA} = \epsilon_{SB} = \epsilon_{SC} = \epsilon_{SV} = 0$; Red: A segments; Blue: B segments; Green: C segments; White: vacancies. (a) $\epsilon_{S0B} = \epsilon_{S21B} = -0.3$, $\epsilon_{S0A} = \epsilon_{S0C} = 0$, $\epsilon_{S21A} = \epsilon_{S21C} = 0$; (b) $\epsilon_{S0B} = \epsilon_{S21B} = -1$, $\epsilon_{S0A} = \epsilon_{S0C} = 0$, $\epsilon_{S21A} = \epsilon_{S21C} = 0$; (c) $\epsilon_{S0B} = \epsilon_{S21B} = -2$, $\epsilon_{S0A} = \epsilon_{S0C} = 0$, $\epsilon_{S21A} = \epsilon_{S21C} = 0$.

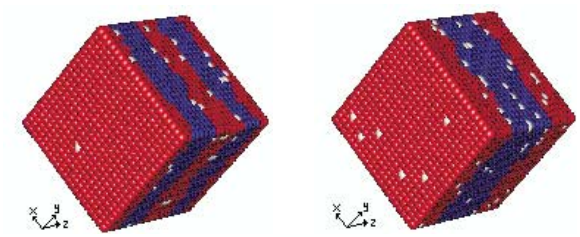

(a) (b)

Fig. 26. Microdomain morphologies of $A_5B_{10}A_5$ and $A_{10}B_{20}A_{10}$ triblock copolymers films for $\epsilon_{SB} = \epsilon_{SV} = 0$, $\epsilon_{SA} = -0.3$, $\epsilon_{AB} = 0.3$, $\epsilon_{AV} = \epsilon_{BV} = 0$ and $\epsilon_{AA} = \epsilon_{BB} = \epsilon_{VV} = 0$. Red: A segments; Blue: B segments; White: vacancies; (a) $A_5B_{10}A_5$, (b) $A_{10}B_{20}A_{10}$.

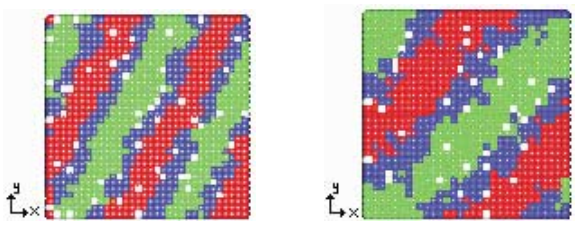

(a) (b)

Fig. 27. Microdomain morphologies of $A_5B_5C_5$ and $A_{10}B_{10}C_{10}$ triblock copolymers films for $\epsilon_{AB} = \epsilon_{AC} = \epsilon_{BC} = 0.3$, $\epsilon_{AA} = \epsilon_{BB} = \epsilon_{CC} = \epsilon_{VV} = 0$, $\epsilon_{AV} = \epsilon_{BV} = \epsilon_{CV} = 0$, and $\epsilon_{SA} = \epsilon_{SB} = \epsilon_{SC} = \epsilon_{SV} = 0$; Red: A segments; Blue: B segments; Green: C segments; White: vacancies; (a) $A_5B_5C_5$, (b) $A_{10}B_{10}C_{10}$.

less sharp. Matsen [28] arrived at a similar conclusion for a bulk system via a SCFT. The beads of the shorter block AI penetrated into the B microdomains in the $A_1B_{10}A_9$ system and occupied several sites on the walls, even when in the symmetric case ($A_5B_{10}A_5$) the walls had enough preference for the B beads to prevent the approaching of the A beads.

In the $A_mB_nC_p$ ($m = p$) systems, the interactions between the different kinds of beads affected as strongly as the composition the microdomain morphologies. When the repulsive interactions between different kinds of beads were not very strong ($\epsilon_{AB} = \epsilon_{AC} = \epsilon_{BC} = 0.3$), an alternate ABCCBA lamellar structure was formed in a wide composition range. By increasing the repulsive interactions between different kinds of beads to $\epsilon_{AB} = \epsilon_{AC} = \epsilon_{BC} = 1$, more complicated patterns were generated. By adjusting the interactions between different kinds of beads, one could generate a large variety of microdomain morphologies. Depending upon the preference of the walls, normal alternate lamellae, parallel lamellae and other special morphologies were formed. For neutral walls, ABCCBA alternate lamellae were normal to the walls. However, when the walls preferred A, lamellae parallel to the walls were formed, whereas, when they preferred B ($\epsilon_{S0B} = \epsilon_{S21B} = -0.3$, $\epsilon_{S0A} = \epsilon_{S21A} = \epsilon_{S0C} = \epsilon_{S21C} = 0$), an ABCCBA normal lamellar structure was generated. The walls were increasingly occupied by the B segments and normal microdomain were formed away from the two walls as the preference for the B segments by the walls increased. The self-consistent field predictions of Pickett and Balazs [40] and the experimental results of Elbs et al. [39] provided the same behavior.

References

[1] Floudas G, Ulrich R, Wiesner U. J Chem Phys 1999;110:652.
[2] Mansky P, Russell TP, Hawker CJ, Mays J, Cook DC, Satija SK. Phys Rev Lett 1997;79:237.
[3] Thomas EL. Science 1999;286:1307.
[4] Park M, Harrison C, Chainkin PM, Register RA, Adamson DH. Science 1997;276:1401.
[5] Albrecht TT, Schotter J, Kästle GA, Emley N, Shibauchi T, Elbaum LK, Guarini K, Black CT, Tuominen MT, Russell TP. Science 2000; 290:2126.
[6] Martins S, Morgado WAM, Massunaga MSO, Bahiana M. Phys Rev E 2000;61:4118.
[7] Zhang HD, Zhang JW, Yang YL, Zhou XD. J Chem Phys 1997;106: 784.
[8] Brown G, Chakrabati A. J Chem Phys 1995;102:1440.
[9] Turner MS. Phys Rev Lett 1992;69:1788.
[10] Lambooy P, Russell TP, Kellogg GJ, Mayes AM, Gallagher PD, Satija SK. Phys Rev Lett 1994;72:2899.
[11] Brown G, Chakrabarti A. J Chem Phys 1995;102(3):1440.
[12] Sommer JU, Hoffmann A, Blumen A. J Chem Phys 1999;111:3728.
[13] Huang E, Russell TP, Harrison C, Chaikin PM, Register RA, Hawker CJ, Mays J. Macromolecules 1998;31:7641.
[14] Kellogg GJ, Walton DG, Mayes AM, Lambooy P, Russell TP, Gallagher PD, Satija SK. Phys Rev Lett 1996;76:2503.
[15] Geisinger T, Müller M, Binder K. J Chem Phys 1999;111:5241. see also p. 5251.
[16] Wang Q, Yan QL, Neeley PF, de Pablo JJ. J Chem Phys 2000;112: 450.
[17] Matsen MW. J Chem Phys 1997;106:7781.
[18] Wang Q, Nealey PF, de Pablo JJ. Macromolecules 2001;34:3458.
[19] Matsen MW, Thompson RB. J Chem Phys 1999;111:7139.
[20] Li B, Ruckenstein E. Macromol Theory Simul 1998;7:333.
[21] Nguyen-Misra M, Misra S, Mattice WL. Macromolecules 1996;29: 1407.
[22] Björling M. Macromolecules 1998;31:9026.
[23] Björling M, Stilbs P. Macromolecules 1998;31:9033.
[24] Mai SM, Mingvanish W, Turner SC, Chaibundit C, Fairclough JPA, Heatley F, Matsen MW, Ryan AJ, Booth C. Macromolecules 2000;33: 5124.
[25] Suh KY, Kim YS, Lee HH. J Chem Phys 1998;108:1253.
[26] Van Dijk MA, Van den Berg R. Macromolecules 1995;28:6773.
[27] Konrad M, Knoll A, Krausch G, Magerle R. Macromolecules 2000; 33:5518.
[28] Matsen MW. J Chem Phys 2000;113:5539.
[29] Nakazawa H, Ohta T. Macromolecules 1993;26:5503.
[30] Zheng W, Wang ZG. Macromolecules 1995;28:7215.
[31] Matsen MW. J Chem Phys 1998;108:785.
[32] Drolet F, Fredrickson GH. Phys Rev Lett 1999;83:4317.
[33] Bohbot-Raviv Y, Wang ZG. Phys Rev Lett 2000;85:3428.
[34] Matsushita Y, Suzuki J, Seki M. Physica B 1998;248:238.
[35] Suzuki J, Seki M, Matsushita Y. J Chem Phys 2000;112:4862.
[36] Shefelbine TA, Vigild ME, Matsen MW, Hajduk DA, Hillmyer MA, Cussler EL, Bates FS. J Am Chem Soc 1999;121:8457.
[37] Hückstädt H, Goldack T, Göpfert A, Abertz V. Macromolecules 2000; 33:3757.
[38] Breiner U, Krappe U, Thomas EL, Stadler R. Macromolecules 1998; 31:135.

[39] Elbs H, Fukunaga K, Stadler R, Sauer G, Magerle R, Krausch G. Macromolecules 1999;32:1204.
[40] Pickett GT, Balazs AC. Macromol Theory Simul 1998;7:249.
[41] Larson RG, Scriven LE, Davis T. J Chem Phys 1985;83:2411.
[42] Reiter J, Edling T, Pakula T. J Chem Phys 1990;93:837.
[43] Lu JM, Yang YL. Chin Sci A 1992;9:1001.
[44] Feng J, Ruckenstein E. Macromol Theory Simul 2002; in press.
[45] Phan S, Fredrickson GH. Macromolecules 1998;31:59.